nature materials

ARTICLES

https://doi.org/10.1038/s41563-020-0634-7

Check for updates

Efficient metal ion sieving in rectifying subnanochannels enabled by metal–organic frameworks

Jun Lu[1,9], Huacheng Zhang[1,9]✉, Jue Hou[1], Xingya Li[1], Xiaoyi Hu[1], Yaoxin Hu[1], Christopher D. Easton[2], Qinye Li[1], Chenghua Sun[3], Aaron W. Thornton[4], Matthew R. Hill[1,2], Xiwang Zhang[1], Gengping Jiang[5]✉, Jefferson Zhe Liu[6], Anita J. Hill[2,4], Benny D. Freeman[7], Lei Jiang[1,8] and Huanting Wang[1]✉

Biological ion channels have remarkable ion selectivity, permeability and rectification properties, but it is challenging to develop artificial analogues. Here, we report a metal–organic framework-based subnanochannel (MOFSNC) with heterogeneous structure and surface chemistry to achieve these properties. The asymmetrically structured MOFSNC can rapidly conduct K^+, Na^+ and Li^+ in the subnanometre-to-nanometre channel direction, with conductivities up to three orders of magnitude higher than those of Ca^{2+} and Mg^{2+}, equivalent to a mono/divalent ion selectivity of 10^3. Moreover, by varying the pH from 3 to 8 the ion selectivity can be tuned further by a factor of 10^2 to 10^4. Theoretical simulations indicate that ion–carboxyl interactions substantially reduce the energy barrier for monovalent cations to pass through the MOFSNC, and thus lead to ultrahigh ion selectivity. These findings suggest ways to develop ion selective devices for efficient ion separation, energy reservation and power generation.

Artificial nanochannel (NC) materials with atomic-level ion selectivity, ultrahigh ion permeability and ion rectification (that is, directional transport) properties comparable to those of biological rectifying ion channels (BRICs) are desirable for high-efficiency separation[1–3] and nanofluidic applications[4–6]. The remarkable ion selectivity of BRICs (that is, rectifying potassium channels[7,8] of K^+/Na^+ selectivity up to 10^4) mainly comes from the ångström-sized and flexible ion selectivity filters[9–11], while the ultrahigh and rectifying ion permeability (~10^8 ions s^{-1} per channel) arises from the heterogeneous pore structures and surface chemistries across the subnanoscale and nanoscale[12–14] (Supplementary Fig. 1a). Inspired by multifunctional BRICs, artificial one-dimensional (1D) solid-state NCs[15,16] have been fabricated to mimic the functionality of BRICs[17]. However, these NCs usually exhibit extremely low selectivity towards metal ions due to their large pore sizes. On the other hand, artificial ångström-sized channels/membranes are expected to mimic the high selectivity of their biological counterparts[17–19]. For example, polymer membranes[20,21] with 0.6- and 1.0-nm-sized 1D channels have been fabricated to achieve K^+/Mg^{2+} selectivities of 40.0 and 16.7, respectively. Reducing the interlayer spacing from ~1.3 to <1 nm (refs. [22,23]) also increased the K^+/Mg^{2+} selectivity of two-dimensional (2D) graphene oxide membranes from ~1 to >650. However, the K^+ transport rates of these 1D and 2D channel membranes decreased by three to four orders of magnitude as the channel diameters decreased from nanometre to subnanometre. Although atomically thin single nanopores[24–26] with pore sizes from 0.5 to >1 nm have been recently fabricated to achieve ultrafast ion transport (>10^8 ions s^{-1} per pore) by graphene and MoS_2 nanosheets, no notable metal ion selectivity or rectification property has been achieved.

In addition to 1D and 2D channel materials, highly water-stable UiO-66 metal–organic frameworks (MOFs)[27,28] have well-defined, three-dimensional (3D) channels consisting of ~6-Å-sized windows and ~8–11-Å-sized cavities and have abundant functional groups on the framework, which may enable them to serve as biomimetic ion filters. However, in contrast with extensive studies of MOFs for molecular separation[29–31], ion transport through MOFs has rarely been investigated. Our recent study demonstrated fast and selective fluoride conduction in positively charged Zr–MOF subnanochannels, formed by completely filling nanochannels in a PET membrane with UiO-66-X (X = H, NH_2 and $N+(CH_3)_3$) MOF crystals[32]; however, these subnanochannels failed to achieve the same level of selectivity as biological fluoride channels because their fluoride selectivity relies on fixed open metal sites on the MOF framework. Moreover, the mechanism of metal ion selective transport in MOFs remains elusive[33,34] and an effective strategy to fabricate highly metal ion selective ion channels is yet to be developed. In view of this, we propose the assembly of 3D porous UiO-66-$(COOH)_2$ into 1D polymer NCs[35,36] to construct asymmetrically structured MOF-based subnanochannels (Asy-MOFSNC) with an ångström-porous MOF

[1]Department of Chemical Engineering, Monash University, Clayton, Victoria, Australia. [2]Manufacturing, CSIRO, Clayton, Victoria, Australia. [3]Department of Chemistry and Biotechnology, Center for Translational Atomaterials, Swinburne University of Technology, Hawthorn, Victoria, Australia. [4]Future Industries, CSIRO, Clayton South MDC, Clayton, Victoria, Australia. [5]College of Science, Wuhan University of Science and Technology, Wuhan, China. [6]Department of Mechanical Engineering, The University of Melbourne, Parkville, Victoria, Australia. [7]Department of Chemical Engineering, The University of Texas at Austin, Austin, TX, USA. [8]Key Laboratory of Bioinspired Materials and Interfacial Science, Technical Institute of Physics and Chemistry, Chinese Academy of Sciences, Beijing, People's Republic of China. [9]These authors contributed equally: Jun Lu, Huacheng Zhang. ✉e-mail: huacheng.zhang@monash.edu; gengpingjiang@wust.edu.cn; huanting.wang@monash.edu

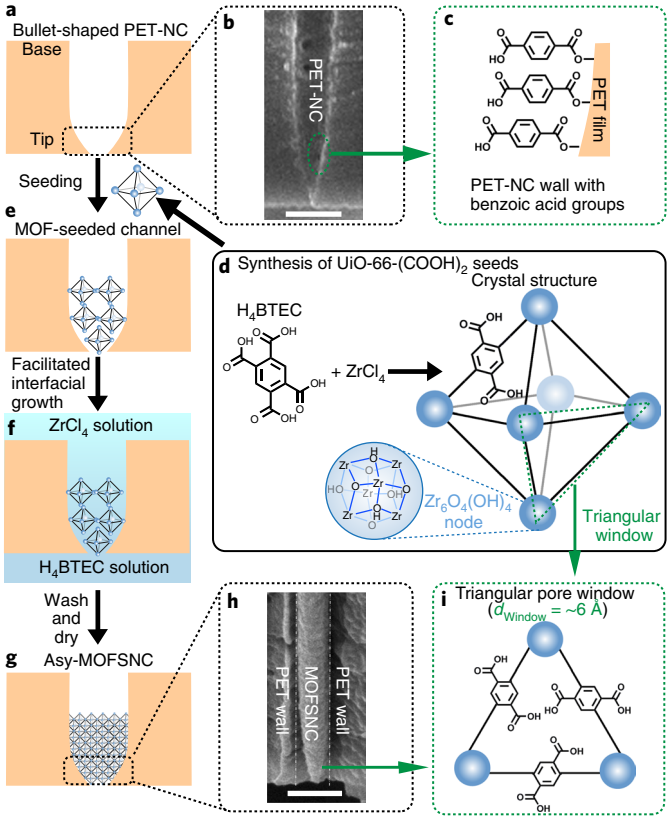

Fig. 1 | Fabrication of Asy-MOFSNC using a facilitated interfacial growth strategy, MOF = UiO-66-(COOH)$_2$. a, Schematic of a single bullet-shaped NC embedded within a PET membrane that has a narrow tip and a wide base. **b**, SEM image of the PET-NC tip region. Scale bar, 500 nm. **c**, Benzoic acid groups on the PET-NC wall. **d**, Synthesis of UiO-66-(COOH)$_2$ nanoparticle seeds. UiO-66-(COOH)$_2$ has subnanometre-to-nanometre porous networks composed of nanometre-sized tetrahedral and octahedral cavities (~8–11 Å in diameter) connected by ångström-sized triangular windows (~6 Å in diameter). **e**, Seeding of MOF nanoparticles into PET-NC. **f**, Facilitated interfacial growth of the UiO-66-(COOH)$_2$ crystals into PET-NC. **g**, Cartoon of the Asy-UiO-66-(COOH)$_2$-SNC membrane. UiO-66-(COOH)$_2$ crystals are mainly assembled adjacent to the tip region of the channel (Supplementary Fig. 4b). **h**, SEM image of local UiO-66-(COOH)$_2$-SNC. Scale bar, 500 nm. **i**, Structure of the triangular window of UiO-66-(COOH)$_2$ with carboxylic groups. d_{Window} indicates pore diameter of the triangular window.

on one side for metal ion sieving and a nanometre-sized region on the other side for fast ion transport (Supplementary Fig. 1b).

Herein, we report a rectifying Asy-MOFSNC for metal ion sieving that shows pH-tunable K^+/Mg^{2+} selectivity between 10^2 and 10^4. Binary ion permeation experiments also confirm that the Asy-UiO-66-(COOH)$_2$-SNC has a much higher K^+/Mg^{2+} selectivity and K^+ permeation rate of 10^5 mol m^{-2} h^{-1} compared with previously reported artificial ion channels/membranes. Molecular dynamics (MD) simulations and density functional theory (DFT) calculations reveal that metal ion transport in MOF channels is associated with dehydration–rehydration effects and ion–COOH interactions, both of which contribute to a high energy barrier for divalent metal ions passing through the MOFSNC, and thus high mono/divalent ion concentrations and mobility ratios in the MOFSNC.

Fabrication of Asy-UiO-66-(COOH)$_2$-SNC

A facilitated interfacial growth strategy was developed to assemble UiO-66-(COOH)$_2$ crystals into single NCs embedded within 12-μm-thick polyethylene terephthalate (PET) membranes to fabricate UiO-66-(COOH)$_2$-SNCs (Fig. 1). The single bullet-shaped NCs with tip and base diameters of 59.2 ± 17.0 nm and 363.3 ± 54.8 nm, respectively, were fabricated using a surfactant-protected ion-track-etching method[37] (Fig. 1a–c and Supplementary Fig. 2). UiO-66-(COOH)$_2$ crystals with an average size of 43.7 nm were synthesized and used as seeds (Fig. 1d and Supplementary Fig. 3a–c). The UiO-66-(COOH)$_2$ seeds had a Brunauer–Emmett–Teller surface area of 405.0 m^2 g^{-1}, comparable to the theoretical accessible surface area of 428.0 m^2 g^{-1} and previous experimental results[38,39]. The pore size distribution profile exhibited an aperture pore size of ~6 Å based on N_2 sorption isotherms (Supplementary Fig. 3d). In the seeding process, the asymmetric shape of the NC favours seeding of the negatively charged MOF nanoparticles into the tip and away from the base when a potential of 2 V is applied to the tip (Fig. 1e). In the interfacial growth process, the tip served as a bottleneck to properly regulate mixing of 1,2,4,5-benzenetetracarboxylic acid (H_4BTEC) molecules and Zr^{4+} ions in the tip region of the PET-NC via counter-diffusion (Fig. 1f). Consequently, nanoconfined nucleation and growth of UiO-66-(COOH)$_2$ were facilitated by the seeded MOF nanocrystals. The benzoic acid groups present on the inner surface of the PET-NC (Fig. 1b,c) served as ligands to synthesize the MOF in the confined PET-NC, which ensures close integration of UiO-66-(COOH)$_2$ crystals with the substrate to eliminate any possible voids between embedded UiO-66-(COOH)$_2$ and the PET-NC wall.

After this interfacial growth process, UiO-66-(COOH)$_2$ crystals were successfully assembled adjacent to the tip region of the PET-NC (Fig. 1g), which was confirmed by scanning electron microscope (SEM) images of the tip, base and cross-section of the MOFSNC, as well as energy-dispersive X-ray spectroscopy (EDX) mapping, X-ray photoelectron spectroscopy (XPS) spectra and powder X-ray diffraction (PXRD) patterns of the PET-NC membranes before and after growth of UiO-66-(COOH)$_2$ (Supplementary Fig. 4). SEM images of the UiO-66-(COOH)$_2$-SNC showed that MOF crystals were highly intergrown in the PET-NC substrate (Fig. 1h). The obtained single Asy-MOFSNC membranes with MOF/polymer hybrid structures were used to study ion transport properties (Fig. 1g–i).

Ultraselective metal ion transport in UiO-66-(COOH)$_2$-SNC

To study the ion transport properties of single PET-NC membranes before and after growth of UiO-66-(COOH)$_2$, current–voltage (I–V) curves were measured in 0.1 M LiCl, NaCl, KCl, $MgCl_2$ and $CaCl_2$ (pH 5.7) aqueous solutions. For pristine PET-NC, asymmetric I–V curves were observed in all electrolyte solutions, indicating that the PET-NC could rectify ion currents and had a preferential direction, from tip to base, for fast transport of positively charged metal ions (Fig. 2a). Ion rectification is mainly ascribed to metal ion concentration gradients inside the bullet-shaped PET-NC induced by deprotonated carboxylic groups on the channel wall, which enhance cation conduction in the tip-to-base direction while restraining cation conduction in the opposite direction[40] (Supplementary Fig. 5a and Supplementary Note 1). Ion currents for the various cation salts in the preferential direction varied from −6.04 to −11.60 nA (corresponding to ~3.78–7.25 × 10^{10} ions passing through the NC per second) and showed little sieving of metal ions in the PET-NC (Fig. 2a). The ion rectification ratio, defined as the ion current from tip to base relative to the current from base to tip, $|I_{-1\ V}|/|I_{+1\ V}|$, is used to characterize the extent of ion rectification. Rectification ratios of monovalent chlorides (LiCl, NaCl, KCl) varied from 14.4 to 17.2, which is higher than the values of ~7.9 for divalent chlorides ($MgCl_2$ and $CaCl_2$) (Supplementary Fig. 5b). These measurements demonstrated that bullet-shaped PET-NCs serve as suitable substrates for Asy-MOFSNCs.

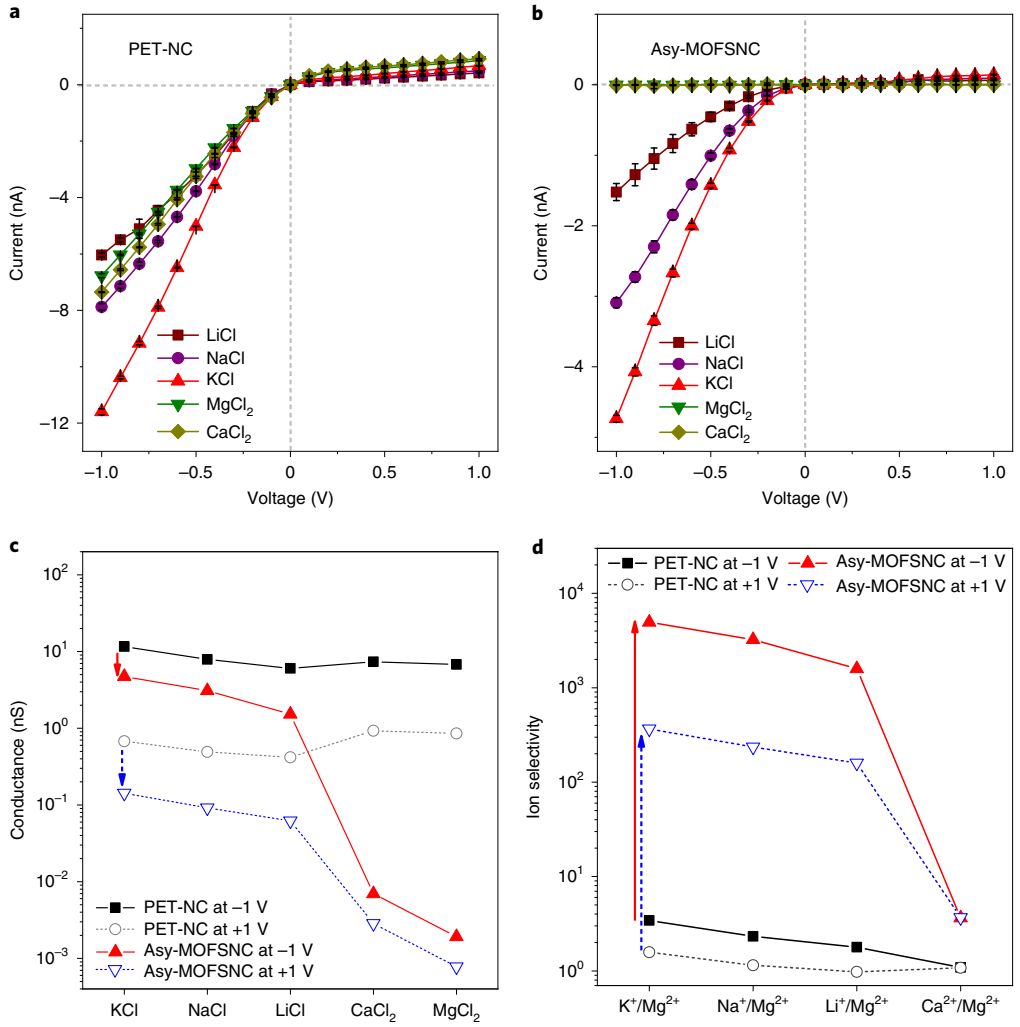

Fig. 2 | Rectifying, ultraselective monovalent metal ion transport in Asy-UiO-66-(COOH)$_2$-SNC. a,**b**, *I*–*V* curves of the bullet-shaped PET-NC before (**a**) and after (**b**) growth of UiO-66-(COOH)$_2$, measured in 0.1 M electrolyte solutions (pH 5.7). Error bars denote 1 s.d. **c**, Ion conductance of PET-NC and Asy-MOFSNC at ±1 V. The monovalent metal ion conductances of the Asy-MOFSNC measured at −1 V are slightly lower than those of the PET-NC substrate, while conductances of divalent metal ions dramatically decline in the Asy-MOFSNC. The Asy-MOFSNC exhibits the following conductance order: $Mg^{2+} < Ca^{2+} \ll Li^{+} < Na^{+} < K^{+}$. **d**, Ion selectivity of the PET-NC and Asy-MOFSNC at ±1 V, calculated using equation (1). K^{+}/Mg^{2+}, Na^{+}/Mg^{2+} and Li^{+}/Mg^{2+} selectivities of the Asy-MOFSNC at −1 V are three orders of magnitude higher than those of the PET-NC.

After modification with UiO-66-(COOH)$_2$, the *I*–*V* curves of the Asy-MOFSNC for monovalent chlorides became much more asymmetric (Fig. 2b). The MOFSNC exhibited much higher rectification ratios (24.6 for LiCl, 33.8 for NaCl, 34.7 for KCl) than those of PET-NC (Supplementary Fig. 5b). This behaviour results from the Asy-MOFSNC having a much greater asymmetry in both surface charge distribution and pore size from tip to base, due to the highly negatively charged and ångström-porous MOF framework in the tip zone compared to that of the PET-NC alone (Supplementary Fig. 5c and Supplementary Note 1). The deprotonation of -COOHs in UiO-66-(COOH)$_2$ was confirmed by its negative Zeta potential of −36.1 ± 1.79 mV in pH 5.7 water (Supplementary Table 1).

Furthermore, the Asy-MOFSNC showed conductance (*G*) values in the following order: $G_{KCl} > G_{NaCl} > G_{LiCl} \gg G_{CaCl_2} > G_{MgCl_2}$ at −1 V, quite different from those of the PET-NC in the same order of magnitude (Fig. 2c). In particular, monovalent metal ion conductances in the Asy-MOFSNC were still of the same order of magnitude as that of the PET-NC. The differences in ion conductances were mainly caused by metal ion conduction differences in the MOFSNC under the same applied voltage, because the salt solutions share the same anion (Cl^{-}). As a result, the K^{+}/Mg^{2+}, Na^{+}/Mg^{2+}, Li^{+}/Mg^{2+} and Ca^{2+}/Mg^{2+} selectivities of the MOFSNC at −1 V (that is, cations driven from tip to base), calculated from equation (1), were 4948.0, 3230.2, 1590.1 and 3.6, respectively, whereas the corresponding selectivities of the PET-NC at −1 V were all below 3.4 (Fig. 2d). Moreover, the K^{+}/Mg^{2+}, Na^{+}/Mg^{2+}, Li^{+}/Mg^{2+} and Ca^{2+}/Mg^{2+} selectivities of the MOFSNC at +1 V (that is, cations driven from base to tip) were 366.4, 235.4, 159.3 and 3.7, respectively.

To confirm the importance of the heterostructure of the Asy-MOFSNC, a uniform MOFSNC (Uni-MOFSNC) was fabricated by symmetrical growth of UiO-66-(COOH)$_2$ crystals covering the entire channel of the PET-NC. Unlike the Asy-MOFSNC, which has high pore size and surface charge asymmetries in the tip-to-base direction, the Uni-MOFSNC had no asymmetry in pore size or surface charge (Supplementary Fig. 5d–f). As a result, the Uni-MOFSNC had no ion rectification effect, evidenced by symmetrical *I*–*V* curves (Supplementary Fig. 5g). In addition, ion conductances and selectivities in the Uni-MOFSNC at −1 V were one order of magnitude lower than that of the Asy-MOFSNC (Supplementary Fig. 5h,i). These results confirm that the heterostructure of the

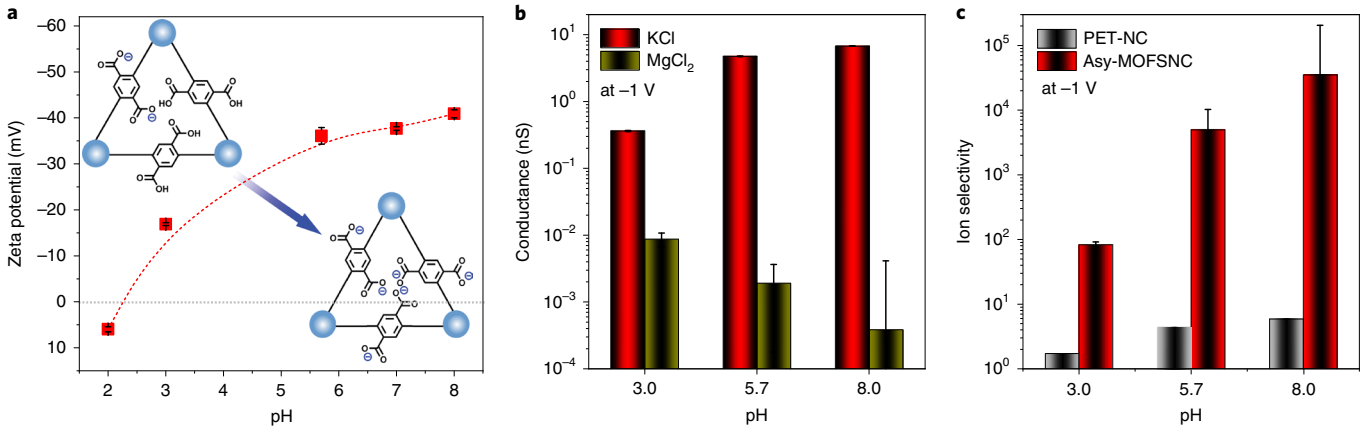

Fig. 3 | pH-dependent mono/divalent ion conductance and selectivity in the Asy-UiO-66-(COOH)$_2$-SNC. a, Zeta potential of UiO-66-(COOH)$_2$ as a function of pH, confirming that the isoelectric point of UiO-66-(COOH)$_2$ is ~2.3. Inset schematics indicate the pH-responsive property of the UiO-66-(COOH)$_2$ pore window. **b**, Influence of pH on KCl and $MgCl_2$ conductance in the Asy-MOFSNC at −1 V. KCl conductance increased with pH, while $MgCl_2$ conductance decreased with pH. **c**, Influence of pH on K^+/Mg^{2+} selectivity of PET-NC and Asy-MOFSNC at −1 V. Error bars denote 1 s.d.

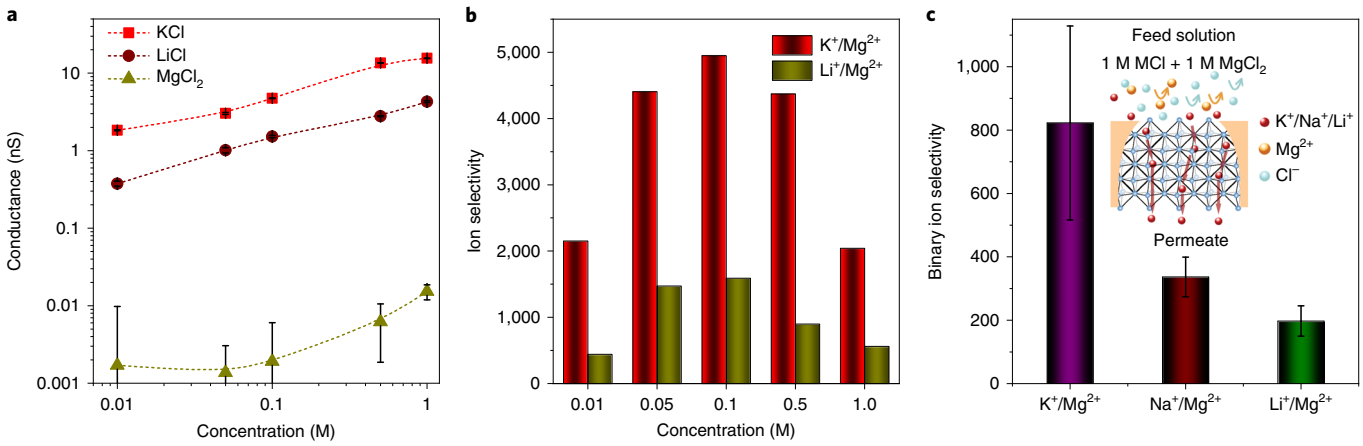

Fig. 4 | Concentration-dependent ion conductance and selectivity, and binary ion selectivity of the Asy-UiO-66-(COOH)$_2$-SNC. a, KCl, LiCl and $MgCl_2$ conductance of the Asy-MOFSNC as a function of ion concentration. **b**, Ion selectivity of the Asy-MOFSNC as a function of ion concentration. The MOFSNC exhibited the highest ion selectivity at 0.1 M. **c**, Binary K^+/Mg^{2+}, Na^+/Mg^{2+} and Li^+/Mg^{2+} selectivities of the Asy-MOFSNC. The inset is a schematic of the binary ion permeation experiments. Error bars represent 1 s.d.

Asy-MOFSNC in the tip-to-base direction is essential for its multiple ion conduction properties.

As shown in Fig. 3a, the Zeta potential of UiO-66-(COOH)$_2$ decreased with increasing pH, and the isoelectric point of UiO-66-(COOH)$_2$ is ~2.3. At pH values above the isoelectric point, the increase in negative Zeta potential with increasing pH means that more of the carboxylic groups in the MOF framework tend to be deprotonated at a high pH (Fig. 3a). pH-responsive *I*–*V* curves of the Asy-MOFSNC are shown in Supplementary Fig. 6a–c. KCl conductance of the Asy-MOFSNC increased sharply from 0.36 to 6.75 nS, whereas $MgCl_2$ conductance decreased dramatically from 8.73 to 0.39 pS as the pH increased from 3 to 8 (Fig. 3b). Correspondingly, the K^+/Mg^{2+} selectivity of the MOFSNC increased from ~10^2 to ~10^4 as the pH increased from 3 to 8 (Fig. 3c). Based on these results, the Asy-MOFSNC demonstrated unprecedented pH-tunable, ultrahigh K^+/Mg^{2+} selectivity.

The dependence of ion conductance on electrolyte concentration was also studied by varying the concentrations of KCl, LiCl and $MgCl_2$ from 0.01 to 1.0 M (Supplementary Fig. 6d–f for *I*–*V* curves at different concentrations). As shown in Fig. 4a, K^+, Li^+ and Mg^{2+} conductance of the MOFSNC increased substantially with ion concentration, and the conductance order measured at the same concentrations was $K^+ > Li^+ » Mg^{2+}$. The K^+/Mg^{2+} selectivity of the Asy-UiO-66-(COOH)$_2$-SNC at −1 V increased from 2,152 to 4,948 as the concentration was increased from 0.01 to 0.1 M, and then decreased to 2,040 as the concentration was increased to 1.0 M (Fig. 4b). The Li^+/Mg^{2+} selectivity of the MOFSNC followed the same trend as the K^+/Mg^{2+} selectivity, and the Li^+/Mg^{2+} selectivity is smaller than the K^+/Mg^{2+} selectivity at the same concentration.

The UiO-66-(COOH)$_2$-SNC had a stable cyclic ion selectivity performance (Supplementary Fig. 7a) due to the superior stability of the MOF in chloride salt solutions, and this is confirmed by the lack of change in the UiO-66-(COOH)$_2$ crystals in terms of crystallinity, shape, size and elemental composition observed using PXRD, SEM and XPS survey spectra (Supplementary Fig. 7b,c and Supplementary Table 2) even after immersion of the MOF crystals in chloride salt solutions for 10 days. Figure 4c shows the binary ion separation results (see details of binary ion permeation experiments

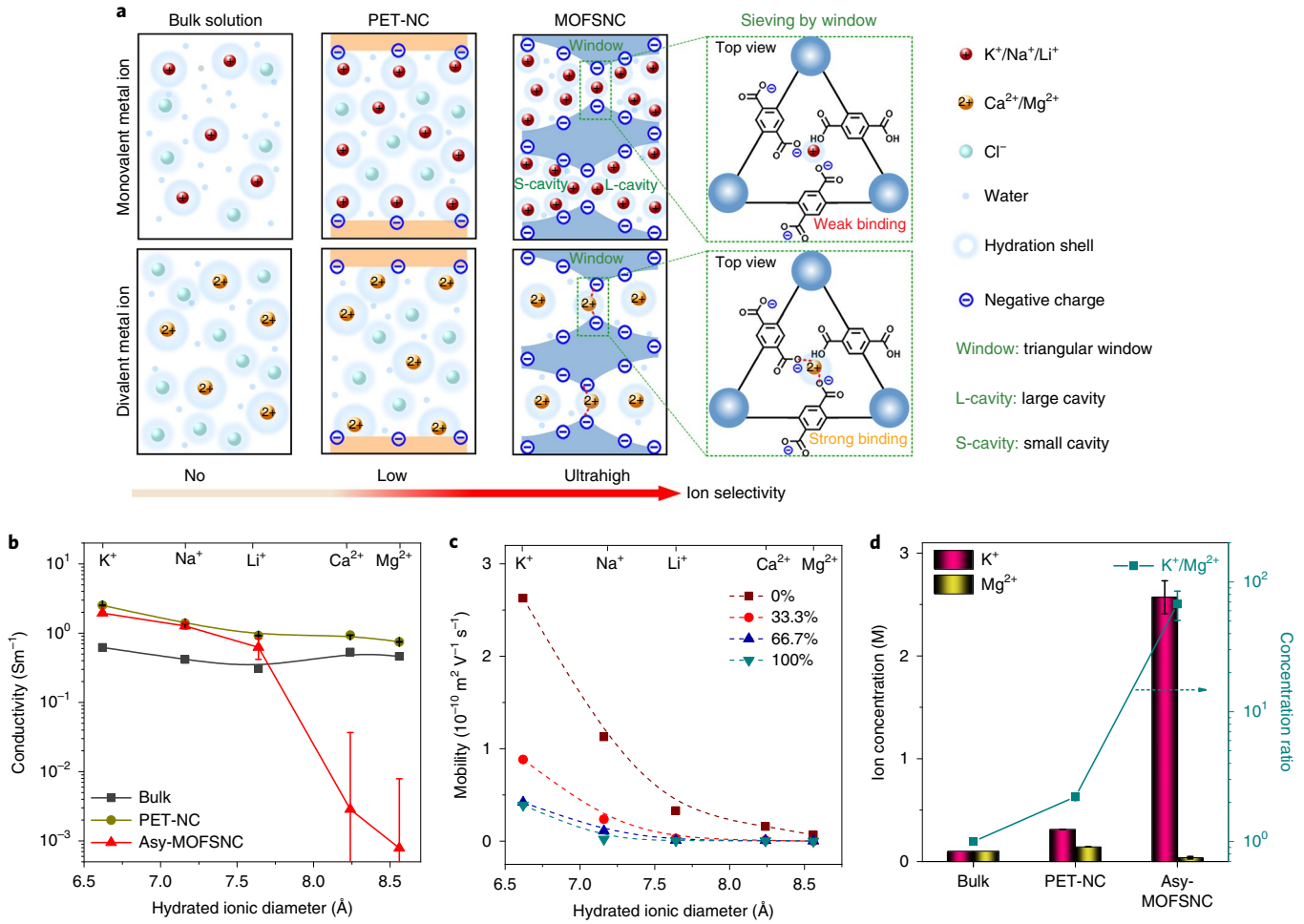

Fig. 5 | Ion sieving mechanism in the UiO-66-(COOH)$_2$-SNC. a, Schematics of three representative ion transport mechanisms in bulk solution (left), slightly negatively charged PET-NC (middle) and highly negatively charged MOFSNC with a cavity-neck architecture (right). Schematic illustration of metal ion transport along the [111] direction of the pathway across the triangular window that connects the small cavity (S-cavity) to the large cavity (L-cavity) in the UiO-66-(COOH)$_2$ framework. Metal ions are mainly sieved by ångström-sized pore windows in the MOFSNC via the partial dehydration effect of metal ions and the short-range ion–MOF interactions. **b**, Ion conductivities in bulk, PET-NC and Asy-MOFSNC measured in 0.1 M electrolyte at −1 V. **c**, Cation mobilities calculated using MD simulations for 0%, 33.3%, 66.7% and 100% deprotonation degrees of free -COOH groups in the flexible UiO-66-(COOH)$_2$ framework. **d**, Experimental $K^+$and Mg^{2+} concentrations and concentration ratios in bulk solution, PET-NC and the MOF framework. Error bars show 1 s.d.

in Methods). The permeation rates for K^+, Na^+ and Li^+ were up to 10^5 mol m^{-2} h^{-1} (Supplementary Table 3), all of which are about four orders of magnitude higher than those of a nanoporous membrane driven identically under a transmembrane voltage bias[20,21,33]. The binary K^+/Mg^{2+} and Na^+/Mg^{2+} selectivities were up to 822.7 and 336.7, respectively (Fig. 4c), which are high when compared with ion separation results by artificial channels or membranes previously reported (Supplementary Table 4).

Mechanism of metal ion selectivity in UiO-66-(COOH)$_2$-SNC

It is well known that ions are hydrated in water (Fig. 5a, left). The five metal ions considered have very similar hydrated ionic diameters and mobilities[41] (Supplementary Table 5). As the pore size of the PET-NC is much larger than the hydrated diameter of the ions under consideration (Fig. 5a, middle), it is difficult to separate them using the PET-NC alone (Fig. 2a, d). Indeed, metal ion mobilities in the PET-NC measured using drift–diffusion experiments are similar to those in the bulk solution (Methods and Supplementary Fig. 8a–c). However, when the concentration of metal ions in the bulk solution on both sides of the NC is set to 0.1 M, metal ion concentrations in the NC are higher than in the bulk solution, due to the electric double layer effect[42] (Supplementary Figs. 5a and 8d). Ion conductivity is defined as $k = 10^3 \mu cF$, where μ is the ion mobility, c is the ion concentration and F is Faraday's constant. Accordingly, metal ion conductivities of the PET-NC are higher than bulk values (Fig. 5b). The Asy-UiO-66-(COOH)$_2$-SNC, however, has a narrow window diameter of ~6 Å, which is smaller than the hydrated ion diameters. The metal ions are likely to be partially dehydrated and interact with carboxylic groups on the MOF framework when passing through these windows (Fig. 5a, right), thus leading to very different ion conductivities, mobilities and concentrations in the MOFSNC (Fig. 5b–d). The dehydration effect was confirmed by MD simulations that showed reduced hydration numbers for metal ions in MOF windows and cavities (Supplementary Figs. 9 and 10). In addition, divalent metal ions have a stronger binding affinity with carboxylic groups on the MOF window than monovalent ions, as estimated by DFT calculations (Supplementary Table 5).

On the basis of the binding affinity and dehydration energy differences between monovalent and divalent cations (Supplementary Table 5), simulated ion mobilities in the uncharged and negatively

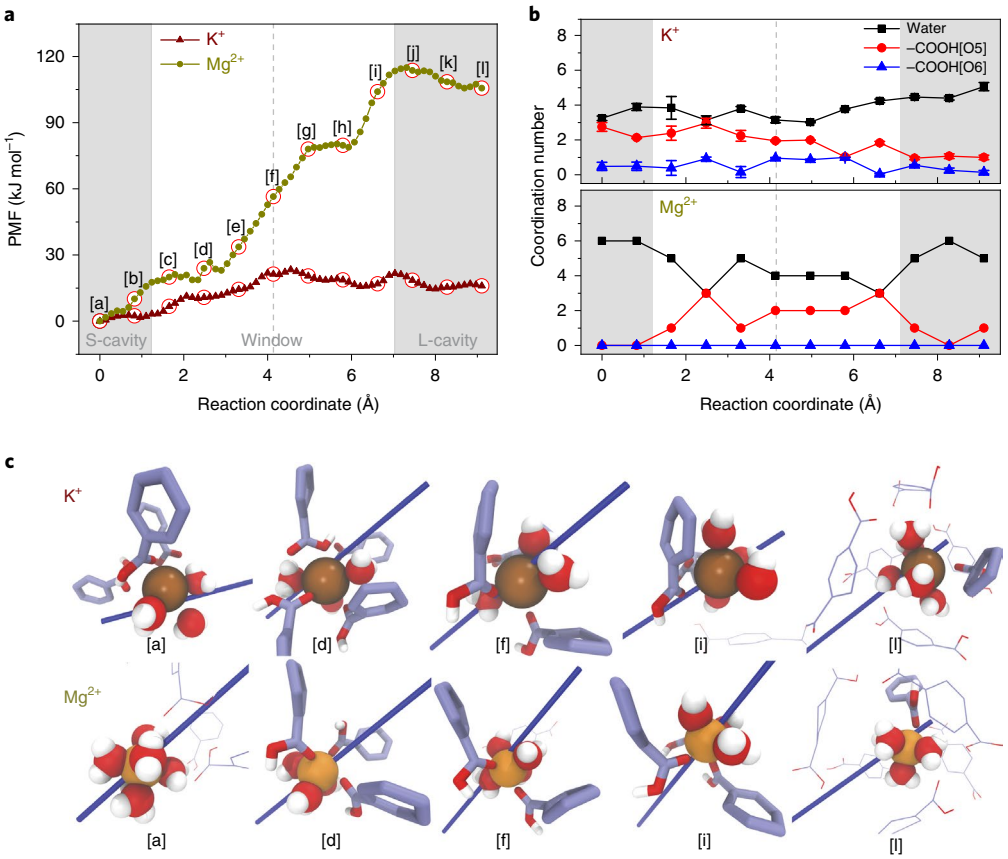

Fig. 6 | Energy barriers, dehydration effects and ion–framework interactions of K^+ and Mg^{2+} in the UiO-66-$(COOH)_2$-SNC. a, PMF for metal ions migrating along the [111] direction through the UiO-66-$(COOH)_2$ framework. The reaction coordinate represents different locations along this pathway in the MOF framework, while the vertical dashed line at 4.14 Å indicates the centre of the subnanometre window. Twelve representative locations (denoted [a]–[l] and marked by red dots) were selected for more detailed analysis; locations [a], [f] and [l] represent the centre of the small cavity, window and large cavity, respectively. **b**, Coordination number of water (black) and -COOH groups (red and blue) for K^+ and Mg^{2+} at the 12 selected locations. O5 and O6 represent two different oxygen atoms in the -COOH group (Supplementary Fig. 9b). In both **a** and **b**, the grey and white areas from left to right indicate the small cavity region, window region and large cavity region, respectively. Error bars denote 1 s.d. **c**, Molecular snapshots of K^+ and Mg^{2+} at locations [a], [d], [f], [i] and [l]. The adjacent organic ligands without ion binding are presented in line style.

charged UiO-66-$(COOH)_2$ framework consistently follow the order $K^+ > Na^+ > Li^+ > Ca^{2+} > Mg^{2+}$ (Fig. 5c), which agrees with the experimental conductivity order of the MOFSNC (Fig. 5b). In our MD simulations, the monovalent metal ion mobility in the MOF framework is two orders of magnitude lower than that in the bulk solution (Supplementary Table 5), because the metal ions spend most of their time oscillating inside the cavities and occasionally jump from one cavity to the next under the external electric field (*E* field). Figure 5c also shows that the ion mobility decreases with increasing deprotonation degree, while the trend remains the same as for the uncharged framework. However, the mono/divalent ion mobility ratio increased with increasing deprotonation degree. Specifically, the K^+/Mg^{2+} mobility ratios were 38.1, 167.5 and 241.6 for 0%, 66.7% and 100% deprotonation degrees, respectively (Supplementary Fig. 11b), which supports the increasing ion selectivity performance of UiO-66-$(COOH)_2$-SNC with increasing pH values. It is worth noting that the ion mobility decreases with increasing deprotonation degree (Fig. 5c). However, owing to the increased ion concentration in the MOFSNC, the theoretical ion conductivity of K^+ would increase by 5.53 and 7.13 times for 66.7% and 100% deprotonation degrees, respectively, which also agrees with our experiments (Fig. 3b).

Different metal ion concentrations inside the MOFSNCs were experimentally observed using an in situ elemental analysis (Supplementary Figs. 12 and 13). For example, in a solution mixture of 0.1 M KCl and 0.1 M $MgCl_2$ (pH 5.7), the average K^+ concentration inside the MOFSNC was 2.57 ± 0.16 M, which is about 25.7 times higher than the bulk K^+ concentration of 0.1 M (Fig. 5d). On the other hand, the Mg^{2+} concentration in the MOFSNC was as low as 0.038 ± 0.012 M, which is much lower than its bulk concentration. The average K^+/Mg^{2+} molar ratio in the MOFSNC was $\sim 67.6 \pm 17.1$. Based on the experimental ion conductivities and concentrations, the experimental K^+ mobility of the Asy-MOFSNC (for 0.1 M KCl, pH 5.7) was calculated to be $7.85 \pm 0.41 \times 10^{-9}$ $m^2\ V^{-1}\ s^{-1}$, which is one order of magnitude higher than the MD simulation value (Fig. 5c), while the K^+ mobility of the Uni-MOFSNC was $4.80 \pm 0.52 \times 10^{-10}$ $m^2\ V^{-1}\ s^{-1}$, which is the same order of magnitude as the average theoretical K^+ mobility. The high K^+ concentration and mobility easily explains the observed high K^+ conductivity in the Asy-MOFSNC, which is not only higher than the bulk value but also comparable to that of the PET-NC, while the extremely low Mg^{2+} conductivity is due to the low Mg^{2+} mobility and concentration in the MOFSNC (Fig. 5c,d). As a result, the high K^+/Mg^{2+} mobility and concentration ratios cooperatively contribute to the ultrahigh K^+/Mg^{2+} selectivity in the Asy-MOFSNC. Moreover, the decreased K^+/Mg^{2+} concentration ratio of 2–14 (Supplementary Fig. 13) at 1.0 M bulk concentration explains the decreased ideal and binary K^+/Mg^{2+} selectivity at high concentration (Fig. 4b,c).

To gain a better insight into the metal ion transport mechanism in the UiO-66-$(COOH)_2$ channels, we calculated the potential of mean force (PMF) profile of cation (that is, Mg^{2+} and K^+) migration along the [111] direction of the UiO-66-$(COOH)_2$ crystal, which crosses the MOF window and connects the large and small cavities (Fig. 6a and Supplementary Note 2). The energy barrier for Mg^{2+} passing through one window (~115.1 kJ mol^{-1}) was five times higher than that of K^+ (~23.3 kJ mol^{-1}). The degree of dehydration and the ion–MOF interaction of the metal ions at 12 representative locations (denoted as [a]–[f] in Fig. 6a) along the pathway were also observed by quantifying the coordination number of the water molecules and -COOHs surrounding the metal ions (Fig. 6b). Locations [a], [f] and [l] represent the centre of the small cavity, window and large cavity, respectively. In contrast to K^+, which has a relatively stable ion–COOH coordination number around 1–4, the Mg^{2+}–COOH coordination number varied between 0 and 3, and the number of water molecules of the first hydration shell varied between 6 and 3. This result indicates that Mg^{2+} must undergo repeated dehydration–rehydration steps when passing through the cavity–window–cavity MOF channel. Moreover, MD simulations also reveal that the UiO-66-$(COOH)_2$ framework is flexible, and the organic ligand units simultaneously rotate with the migration of metal ions in the MOF channel. In particular, the conformational change of -COOH groups enables continuous binding interaction with the K^+ ion and smaller variation of its water hydration number along the subnanometre channel, which accounts for its lower energy barrier (Fig. 6b,c and Supplementary Fig. 14–16). Overall, the selective mechanisms of the MOFSNC share some interesting features analogous to biological ion channels, such as the dehydration effect, the specific interaction between K^+ ions and carbonyl groups, and the structural flexibility of the biological K^+ channels[8,9,12].

Outlook

Rectifying MOFSNCs with a hybrid heterostructure from 3D subnanoporous materials to 1D nanoscale ion channels have been successfully prepared and achieve ultrahigh, pH-tunable monovalent metal ion selectivity and permeability. Our experimental and theoretical simulation results reveal the dehydration–rehydration effect and interactions between ions and the flexible carboxyl ligands of the MOF are two key factors for ultraselective and ultrafast metal ion transport in MOFSNCs, because they lead to ultrahigh mono/divalent cation mobility and concentration ratios within them. Our work demonstrates that the design of the channel materials with multiple length scales and pore dimensions is an effective way to construct artificial multifunctional ion channels with a desirable combination of selectivity, permeability and rectification properties, which is different from previously reported single-scale and single-dimensional channels. Using this design strategy, more MOF-based artificial ion channels, such as potassium, sodium, calcium and magnesium channels with multifunctionality comparable to their biological counterparts, will probably be realized in the future. Given the rectifying, ultrafast, ultraselective and pH-tunable ion transport properties, our work opens a new pathway for the development of diverse multifunctional ion channel membranes for applications such as efficient ion separation and power generation.

Online content

Any methods, additional references, Nature Research reporting summaries, source data, extended data, supplementary information, acknowledgements, peer review information; details of author contributions and competing interests; and statements of data and code availability are available at https://doi.org/10.1038/s41563-020-0634-7.

Received: 29 January 2019; Accepted: 7 February 2020;
Published online: 09 March 2020

References

1. Radha, B. et al. Molecular transport through capillaries made with atomic-scale precision. *Nature* **538**, 222–225 (2016).
2. Blankenburg, S. et al. Porous graphene as an atmospheric nanofilter. *Small* **6**, 2266–2271 (2010).
3. Cohen-Tanugi, D. & Grossman, J. C. Water desalination across nanoporous graphene. *Nano Lett.* **12**, 3602–3608 (2012).
4. Sparreboom, W., van den Berg, A. & Eijkel, J. C. Principles and applications of nanofluidic transport. *Nat. Nanotechnol.* **4**, 713–720 (2009).
5. Feng, J. et al. Single-layer MoS_2 nanopores as nanopower generators. *Nature* **536**, 197–200 (2016).
6. Li, R., Fan, X., Liu, Z. & Zhai, J. Smart bioinspired nanochannels and their applications in energy-conversion systems. *Adv. Mater.* **29**, 1702983 (2017).
7. Catterall, W. A. Structure and function of voltage-sensitive ion channels. *Science* **242**, 50–61 (1988).
8. MacKinnon, R. Potassium channels and the atomic basis of selective ion conduction (Nobel lecture). *Angew. Chem. Int. Ed.* **43**, 4265–4277 (2004).
9. Doyle, D. A. et al. The structure of the potassium channel: molecular basis of K^+ conduction and selectivity. *Science* **280**, 69–77 (1998).
10. Gulbis, J. M., Mann, S. & MacKinnon, R. Structure of a voltage-dependent K^+ channel β subunit. *Cell* **97**, 943–952 (1999).
11. Gouaux, E. & MacKinnon, R. Principles of selective ion transport in channels and pumps. *Science* **310**, 1461–1465 (2005).
12. Zhou, Y., Morais-Cabral, J. H., Kaufman, A. & MacKinnon, R. Chemistry of ion coordination and hydration revealed by a K^+ channel–Fab complex at 2.0 Å resolution. *Nature* **414**, 43–48 (2001).
13. Roux, B. & MacKinnon, R. The cavity and pore helices in the KcsA K^+ channel: electrostatic stabilization of monovalent cations. *Science* **285**, 100–102 (1999).
14. Nishida, M. & MacKinnon, R. Structural basis of inward rectification: cytoplasmic pore of the G protein-gated inward rectifier GIRK1 at 1.8 Å resolution. *Cell* **111**, 957–965 (2002).
15. Zhang, H. et al. Bioinspired smart gate-location-controllable single nanochannels: experiment and theoretical simulation. *ACS Nano* **9**, 12264–12273 (2015).
16. Lepoitevin, M., Ma, T., Bechelany, M., Janot, J.-M. & Balme, S. Functionalization of single solid state nanopores to mimic biological ion channels: A review. *Adv. Colloid Interface Sci.* **250**, 195–213 (2017).
17. Tagliazucchi, M. & Szleifer, I. Transport mechanisms in nanopores and nanochannels: can we mimic nature? *Mater. Today* **18**, 131–142 (2015).
18. Amiri, H., Shepard, K. L., Nuckolls, C. & Hernández Sánchez, Rl Single-walled carbon nanotubes: mimics of biological ion channels. *Nano Lett.* **17**, 1204–1211 (2017).
19. He, Z., Zhou, J., Lu, X. & Corry, B. Bioinspired graphene nanopores with voltage-tunable ion selectivity for Na^+ and K^+. *ACS Nano* **7**, 10148–10157 (2013).
20. Wen, Q. et al. Highly selective ionic transport through subnanometer pores in polymer films. *Adv. Funct. Mater.* **26**, 5796–5803 (2016).
21. Wang, P. et al. Ultrafast ion sieving using nanoporous polymeric membranes. *Nat. Commun.* **9**, 569 (2018).
22. Joshi, R. et al. Precise and ultrafast molecular sieving through graphene oxide membranes. *Science* **343**, 752–754 (2014).
23. Abraham, J. et al. Tunable sieving of ions using graphene oxide membranes. *Nat. Nanotechnol.* **12**, 546–550 (2017).
24. Rollings, R. C., Kuan, A. T. & Golovchenko, J. A. Ion selectivity of graphene nanopores. *Nat. Commun.* **7**, 11408 (2016).
25. Feng, J. et al. Observation of ionic coulomb blockade in nanopores. *Nat. Mater.* **15**, 850–855 (2016).
26. Esfandiar, A. et al. Size effect in ion transport through angstrom-scale slits. *Science* **358**, 511–513 (2017).
27. Furukawa, H., Cordova, K. E., O'Keeffe, M. & Yaghi, O. M. The chemistry and applications of metal–organic frameworks. *Science* **341**, 1230444 (2013).
28. Cavka, J. H. et al. A new zirconium inorganic building brick forming metal organic frameworks with exceptional stability. *J. Am. Chem. Soc.* **130**, 13850–13851 (2008).
29. Li, J.-R., Sculley, J. & Zhou, H.-C. Metal–organic frameworks for separations. *Chem. Rev.* **112**, 869–932 (2011).
30. Denny, M. S. Jr, Moreton, J. C., Benz, L. & Cohen, S. M. Metal–organic frameworks for membrane-based separations. *Nat. Rev. Mater.* **1**, 1–17 (2016).
31. Rodenas, T. et al. Metal–organic framework nanosheets in polymer composite materials for gas separation. *Nat. Mater.* **14**, 48–55 (2015).
32. Li, X. et al. Fast and selective fluoride ion conduction in sub-1-nanometer metal–organic framework channels. *Nat. Commun.* **10**, 2490 (2019).
33. Guo, Y., Ying, Y., Mao, Y., Peng, X. & Chen, B. Polystyrene sulfonate threaded through a metal–organic framework membrane for fast and selective lithium-ion separation. *Angew. Chem. Int. Ed.* **55**, 15120–15124 (2016).
34. Zhang, H. et al. Ultrafast selective transport of alkali metal ions in metal organic frameworks with subnanometer pores. *Sci. Adv.* **4**, eaaq0066 (2018).

35. Guo, W., Tian, Y. & Jiang, L. Asymmetric ion transport through ion-channel-mimetic solid-state nanopores. *Acc. Chem. Res.* **46**, 2834–2846 (2013).
36. Zhang, H., Tian, Y. & Jiang, L. Fundamental studies and practical applications of bio-inspired smart solid-state nanopores and nanochannels. *Nano Today* **11**, 61–81 (2016).
37. Wang, J. et al. Oscillatory reaction induced periodic C-quadruplex DNA gating of artificial ion channels. *ACS Nano* **11**, 3022–3029 (2017).
38. Yang, Q. Y. et al. A water stable metal–organic framework with optimal features for CO_2 capture. *Angew. Chem. Int. Ed.* **52**, 10316–10320 (2013).
39. Ragon, F. et al. Acid-functionalized UiO-66(Zr) MOFs and their evolution after intra-framework cross-linking: structural features and sorption properties. *J. Mater. Chem. A* **3**, 3294–3309 (2015).
40. Ramírez, P., Apel, P. Y., Cervera, J. & Mafé, S. Pore structure and function of synthetic nanopores with fixed charges: tip shape and rectification properties. *Nanotechnology* **19**, 315707 (2008).
41. Nightingale, E. Jr Phenomenological theory of ion solvation. Effective radii of hydrated ions. *J. Phys. Chem.* **63**, 1381–1387 (1959).
42. Apel, P. Y., Blonskaya, I. V., Orelovitch, O. L., Ramirez, P. & Sartowska, B. A. Effect of nanopore geometry on ion current rectification. *Nanotechnology* **22**, 175302 (2011).

Methods

Preparation of Asy-UiO-66-$(COOH)_2$-SNC using a facilitated interfacial growth strategy. A facilitated interfacial growth strategy was developed to assemble UiO-66-$(COOH)_2$ into the PET-NCs. Here 0.1 g of UiO-66-$(COOH)_2$ crystals synthesized using the hydrothermal method (Supplementary Information) were dispersed into 10 ml of MilliQ water and sonicated for 1 h before being put into two cells separated by a PET-NC membrane. Driven under −2 V for 20 min, the UiO-66-$(COOH)_2$ seed particles migrated and then deposited into the nanochannel. After washing with distilled water to remove seeds attached to the membrane surface, the seeded PET-NC membrane was clamped into a home-made interfacial synthesis apparatus consisting of two cells, one of which was filled with 5 ml of $ZrCl_4$ (0.35 g) aqueous solution and the other with 5 ml of H_4BTEC (0.38 g) aqueous solution. The interfacial synthesis equipment was then sealed into a polytetrafluoroethylene (PTFE)-lined autoclave, transferred into a preheated oven maintained at 100 °C for 48 h under static conditions. When the interfacial synthesis ended, the MOF modified PET-NC membrane was taken out, washed with distilled water and finally dried at room temperature.

Current measurement. The ionic transport properties of both PET-NC and MOFSNC membranes were studied using *I*–*V* curves. Ionic currents were measured by a Keithley 6487 picoammeter (Keithley Instruments) using an apparatus with two PTFE chambers, which were separated by either a piece of PET-NC or a MOFSNC membrane. The two chambers were filled with chloride salt solutions at the same concentration. Ag/AgCl electrodes in each chamber were used to apply an electric potential across the PET-NC or MOFSNC membranes. Positive voltage values corresponded to the potential being applied to the base of the membranes. The main transmembrane potential used in this work was a scanning voltage that varied from −1 to +1 V. The pH of the electrolyte solutions was adjusted using 0.1 M HCl and 0.1 M KOH solutions. Current measurements at all pH values were carried out at room temperature. Each test was repeated at least three times to get the average current values at different voltages.

Binary ion permeation experiments. The UiO-66-$(COOH)_2$-SNC membrane was clamped between two PTFE compartments, of which one cell, facing the tip of the UiO-66-$(COOH)_2$-SNC, was filled with a binary ion solution containing 10 ml of 1.0 M MCl (LiCl, NaCl or KCl) and 1.0 M $MgCl_2$ as the feed solution, while the other cell was filled with 10 ml of MilliQ water as the permeate solution. The binary ion selectivity test was conducted by applying a constant potential of 1 V via a Keithley 6487 picoammeter across the UiO-66-$(COOH)_2$-SNC membrane for 48 h using Pt electrodes, with both compartments gently magnetically stirred to eliminate concentration gradients. At the end of these experiments, the ion concentrations in the permeate side were measured using inductively coupled plasma optical emission spectrometry.

Ion selectivity based on ion currents. For quantitative comparison, the selectivity ratio (SR) of alkali metal ions over alkali-earth metal ions is calculated as the ratio of respective current at the same transmembrane voltage (that is, −1 or +1 V) according to equation (1), taking into consideration the valence difference:

$$\mathrm{SR}_{\mathrm{MCl/M^{*}Cl_2}} = \left|\frac{I_{\mathrm{MCl}}}{I_{\mathrm{M^{*}Cl_2}}}\right| \times \frac{z_{\mathrm{M^{*}}}}{z_{\mathrm{M}}} \tag{1}$$

where I_{MCl} and $I_{\mathrm{M^{*}Cl_2}}$ are the currents of the alkaline metal chloride electrolytes and alkaline earth metal chloride electrolytes, respectively, at the same concentration; z_{M} and $z_{\mathrm{M^{*}}}$ are the valences of the alkaline and alkaline earth metal ions, respectively.

Ion conductivity in PET-NC and UiO-66-$(COOH)_2$-SNC. The ion conductivity (κ) of a PET-NC can be defined as

$$\kappa = \frac{I}{U} \times \frac{L}{S} \tag{2}$$

where *I* is the ionic current measured at the applied voltage *U*, *S* is the cross-sectional area of the nanochannel and *L* is the length of the NC. For MOFSNCs, *S* is the cross-sectional area of the MOF layers, which is equal to the effective area of the PET-NC.

The radius profile $r(x)$ for the bullet-shaped nanochannel can be described as

$$r(x) = \frac{r_{\mathrm{b}} - r_{\mathrm{t}}\exp(-\frac{L}{h}) - (r_{\mathrm{b}} - r_{\mathrm{t}})\exp(-\frac{x}{h})}{1 - \exp(-\frac{L}{h})} \tag{3}$$

where r_{b} is the base radius, r_{t} is the tip radius, *L* is the nanochannel length and *h* is a geometrical parameter characterizing the curvature of the nanochannel profile, called the curvature radius; *h* was measured by fitting the experimental tip profiles (that is, equation (3))[42]. *L*/*S* of the bullet-shaped nanochannel is theoretically described as

$$\frac{L}{S} = \int_0^L \frac{1}{\pi r^2(x)}\mathrm{d}x = \int_0^L \frac{1}{\pi\left[\frac{r_{\mathrm{b}} - r_{\mathrm{t}}\exp(-\frac{L}{h}) - (r_{\mathrm{b}} - r_{\mathrm{t}})\exp(-\frac{x}{h})}{1-\exp(-\frac{L}{h})}\right]^2}\mathrm{d}x \tag{4}$$

However, the effective area of a single NC is generally estimated using an electrochemical method, mainly because it is difficult to simultaneously and directly measure the geometric parameters (including r_{b}, r_{t} and *h*) of the single NC embedded within a large membrane, using SEM. At high electrolyte concentrations (such as 2.0 M) and a pH lower than the isoelectric point of the surface (3.8 for PET-NC), the electric double layer effect is negligible, so the specific ion conductivity in the nanochannel is equal to that in the bulk solution. Thus, the (*L*/*S*) of PET-NC can be calculated by

$$\left(\frac{L}{S}\right) = \kappa\frac{U}{I} \tag{5}$$

where κ is the ionic conductivity of the 2.0 M electrolyte (pH = 2) in bulk solution and *I* is the ion current of the 2.0 M electrolyte in the PET-NC measured at the applied voltage *U*. By combining the *L*/*S* data of the PET-NC with the corresponding *I*–*V* data, the chloride salt conductivity in the PET-NC and MOFSNC can be obtained using equation (2). It is worth noting that the ion conductivity of the MOFSNC calculated based on the effective area of the PET-NC is the 'device' conductivity of the single MOFSNC (also equivalent to the 'material' ion conductivity of the MOF framework) rather than the actual ion conductivity of the MOF pores. As UiO-66-$(COOH)_2$ is a class of porous material, its effective volume for ion transport is much smaller than the total volume of the MOF crystal itself, as confirmed by the experimental UiO-66-$(COOH)_2$ pore volume of 0.17 $\mathrm{cm^3\,g^{-1}}$ (Supplementary Fig. 3). However, the actual volume of the MOF for ion transport in aqueous environments might be very different from the pore volume observed by measuring N_2 adsorption in the dry state. Therefore, we ultimately used the total volume of MOF crystals to calculate ion concentration in the MOFSNC. If we assume that the length of ion transport in the MOFSNC is constant at the PET membrane thickness of 12 µm, the effective area of the MOFSNC for ion transport should be much smaller than the effective area of the PET-NC, because the effective area of the single PET-NC is the same as the total cross-sectional area of the MOFSNC (Fig. 1a, g). As a result, ion conductivity in the MOFSNC calculated based on the total volume of the MOF framework should be smaller than the actual ion conductivity of the MOF pores. Accordingly, ion concentration in the MOFSNC, defined as the molar quantity of ions divided by the total volume of the MOFSNC, is smaller than the value defined as the molar quantity of ions relative to the effective volume of the MOF pores.

Ion mobility in PET-NC. Drift–diffusion experiments were performed with applied voltages from −0.4 V to 0.4 V versus Ag/AgCl electrodes. The PET-NC membrane was clamped between two chambers, one of which, facing the tip, was filled with 1.0 M chloride salt solution and the other, facing the base, was filled with the same chloride salt solution at a concentration of 0.1 M (Supplementary Fig. 8a). The concentration gradient of electrolyte (Δ) across the membrane was 10. From the resulting *I*–*V* curves (Supplementary Fig. 8b), the measured reverse potential (that is, zero-current potential, E_{m}) was obtained. During these measurements, a redox potential was generated at the electrodes because of the concentration gradient across the membrane; thus E_{m} is subtracted from the redox potential E_{redox}, which is calculated[43] as follows:

$$E_{\mathrm{redox}} = \frac{RT}{zF}\ln\Delta\frac{\gamma_{C_{\mathrm{H}}}}{\gamma_{C_{\mathrm{L}}}} \tag{6}$$

where *R*, *T*, *z* and *F* are the universal gas constant, temperature, ion valence and the Faraday constant, respectively. The γ_C with subscript H and L stands for the activity coefficient of the high concentration (1.0 M) and low concentration (0.1 M), respectively. Thereafter, the real reverse potential E_{R} was calculated by

$$E_{\mathrm{R}} = E_{\mathrm{m}} - E_{\mathrm{redox}} \tag{7}$$

Based on E_{R}, the mobility ratio of cation (μ_+) to anion (μ_-) can be obtained following the Henderson equation[44,26], taking the valence of the cation (z_+) and anion (z_-) into consideration:

$$\frac{\mu_+}{\mu_-} = -\left(\frac{z_+}{z_-}\right)\left(\frac{\ln\Delta - z_- FE_{\mathrm{R}}/RT}{\ln\Delta - z_+ FE_{\mathrm{R}}/RT}\right) \tag{8}$$

For negatively charged nanochannels, the overall ion conductivity can be calculated by

$$\kappa = 10^3(\mu_+ c_+ + \mu_- c_-)N_{\mathrm{A}}e \tag{9}$$

where c_+ and c_- are cation and anion concentrations in the NC, respectively, and N_{A} and *e* are the Avogadro constant and the electron charge, respectively. When the applied voltage is close to zero, the cation concentration in the negatively charged

PET-NC can be calculated as the superimposition of the bulk concentration (c_0) and the counterion concentration induced by the excess negative surface charges (c_s)[45].

$$c_+ = c_0 + c_s \tag{10}$$

$$c_S = 10^{-3}\frac{4\sigma_s}{N_A e d} \tag{11}$$

where d and σ_s are the average pore diameter and effective surface charge density of the PET-NC, respectively. At the same time, the anion concentration inside the PET-NC is equal to the bulk concentration ($c_- = z_+c_0$, $z_+ = 1$ or 2). Therefore, the chloride salt conductivity of the PET-NC can be described as[46]

$$\kappa = 10^3(\mu_+ + z_+\mu_-)c_0 N_A e + \frac{4\mu_+\sigma_s}{d} \tag{12}$$

By combining equation (8) with (12), we can calculate metal ion mobility values in the PET-NC. Based on the experimental chloride salt conductivities in the PET-NC and the experimental ion mobility, the metal ion conductivities of the PET-NC were then calculated using $\kappa_+ = \mu_+\kappa/(\mu_+ + z_+\mu_-)$.

MD simulations. To simulate the electro-kinetic transport inside the UiO-66-$(COOH)_2$ framework, we constructed supercells composed of 3×3×3 UiO-66-$(COOH)_2$ unit cells (Supplementary Fig. 9a). The periodic boundary conditions were applied in all three directions. The supercells were then filled with different types of aqueous electrolyte. A series of MD simulations was carried out to determine the numbers of water molecules in the supercells under thermodynamic equilibrium conditions at 300 K and ~1 atm (see Supplementary Information for details). To model the deprotonation of the -COOH groups at high pH values (for example pH = 5.7 and 8), we removed the H atoms on the -COOH groups and made the UiO-66-$(COOH)_2$ framework negatively charged. Three different deprotonation degrees were considered, that is, 33.3%, 66.7% and 100%. We considered different electrolyte systems, such as LiCl, NaCl, KCl, $MgCl_2$ and $CaCl_2$. For the neutral framework, every unit cell includes one cation–ion pair, corresponding to an ion centration of 0.81 M. For the negatively charged framework, only cations were included in order to make the whole system charge neutral. In our molecular models, the UiO-66-$(COOH)_2$ framework is flexible.

The force model developed by Wu et al.[47] was adopted to describe the flexible UiO-66-$(COOH)_2$ structure. Details of this force model and related parameters are summarized in the Supplementary Information. The non-bonding interactions between electrolyte and UiO-66-$(COOH)_2$ include van der Waals and Coulomb interactions. The 12–6 Lennard-Jones (LJ) potential was used to describe the van der Waals interaction. Supplementary Table 6 summarizes the LJ parameters and the Lorentz–Berthelot mixing rule was used to determine the LJ parameters between different atoms. Most of the LJ parameters of the MOF atoms were taken from the DREIDING force model[48]. The parameters of the Zr atom were obtained from the universal force field model[49]. The LJ parameters of the electrolyte ions were taken from the work of Li and colleagues[50,51], which, to ensure consistency, contains most of the mono and divalent cations in our experiments. In that work, the LJ parameters were fitted to the hydration free energy. These parameters yielded a small discrepancy of hydration free energy (0.1–1%) and hydration shell diameters (1.0–6.7%) between the simulation and experimental results, which is essential to simulate ion transport through subnanometre UiO-66-$(COOH)_2$ windows via partial dehydration. We adopted the TIP3P water model with the SHAKE algorithm.

To determine ion transport mobility, we applied a constant electric field along the [111] crystal direction. Note that in these simulations one Zr atom was fixed and the linear momentum of the whole MOF framework was set at zero to prevent possible drift of the entire structure. From MD simulations, we can calculate the average ion drift velocity along the E-field direction. From the ratio of velocity over E-field strength, we can determine the ion mobility (see Supplementary Information for details). The electro-kinetic mobility of cations and anions inside the UiO-66-$(COOH)_2$ framework was calculated as follows:

$$\mu = \frac{\overline{v_d}}{qE} = \sum_{i=1}^{N}\frac{\sqrt{3}}{3}\frac{(S_{ix} + S_{iz} + S_{iy})}{qNE\Delta t} \tag{13}$$

where $\overline{v_d}$ is the average drift velocity of ions along the E-field direction, q is the ion valence charge, E is the strength of the electric field, Δt is the elapsed time duration, N is the total number of the same type of ions in the system and S_{ix}, S_{iz} and S_{iy} are the total unwrapped displacement of ions along the x, y or z axis for the ith ions, respectively. The $(S_{ix} + S_{iz} + S_{iy})$ is the unwrapped displacement of ions along the [111] direction, along which the external E field was applied.

Values for the PMF of cation migration along the [111] direction that crosses the MOF window and connects the large and small cavities were calculated by using the collective variable module in the LAMMPS software[52]. The simulation systems for PMF calculations were the same as our previous ion mobility study, except that one cation–anion pair was included in the whole system. The cation (K^+ or Mg^{2+}) was confined along the transport pathway (that is, the [111] direction) using a 167.4 kJ mol^{-1} Å^{-2} harmonic restraint. For each cation, 34 umbrella sampling windows were employed on the pathway with a sampling point spacing of about 0.27 Å from the centre of a small cavity to that of a large cavity. For every case, with the cation initially fixed at the harmonic centre, a canonical (constant particle, volume, temperature, NVT) MD simulation was run for 2 ns using a Nosé–Hoover thermostat at 300 K. After that, the cation was released under the constraint of the harmonic spring for an extra 5 ns in the NVT MD simulation. The trajectory of the cation was recorded every 1,000 fs for umbrella sampling. Then, the weighted histogram analysis method was employed to calculate the PMF free-energy results. Figure 6 shows the results for both K^+ and Mg^{2+}.

Our MD simulations were performed using LAMMPS software. The time step for all MD simulations was set as 1 fs. A Nosé–Hoover thermostat was adopted in most cases. For ion mobility simulations, we ran the MD simulations for 12 ns, and the results of ion drift in the last 10 ns were used for analysis. For ion hydration shell analysis, we ran the MD simulations for 8 ns and the results of ion drift in the last 5 ns were used for analysis.

Measurement of K^+/Mg^{2+} concentration ratio in Asy-MOFSNC. A multiple UiO-66-$(COOH)_2$-SNC membrane (with a channel density of 10^8 cm^{-2}) was clamped between two PTFE compartments; both cells were filled with 10 ml of the same electrolyte solution containing either 0.1 M $MgCl_2$ + 0.1 M KCl or 1.0 M $MgCl_2$ + 1.0 M KCl mixture solution with a pH of 5.7. A constant transmembrane voltage of −1.0 V was applied across the membrane for 1 h via a Keithley 6487 picoammeter (Keithley Instruments) using Pt electrodes to ensure that the quantity of metal ions inside the MOFSNC was balanced, as shown in Supplementary Fig. 12a. SEM energy-dispersive X-ray elemental analysis was conducted on cross-sections of the treated UiO-66-$(COOH)_2$-SNC membranes to semiquantify the K/Mg molar ratio in the MOFSNC. Based on the fact that the Zr herein actually comes from the UiO-66-$(COOH)_2$ crystals with high crystallinity, we calculated the concentrations of K^+ and Mg^{2+} according to the K/Zr ratio, Mg/Zr ratio and Zr concentration in the MOFSNC (Supplementary Figs. 12 and 13).

Data availability

All relevant source data within the article and the Supplementary Information are available for download through figshare (https://doi.org/10.6084/m9.figshare.11678046). Additional data related to the paper may be requested from the authors.

References

43. Tunuguntla, R. H. et al. Enhanced water permeability and tunable ion selectivity in subnanometer carbon nanotube porins. *Science* **357**, 792–796 (2017).
44. Perram, J. W. & Stiles, P. J. On the nature of liquid junction and membrane potentials. *Phys. Chem. Chem. Phys.* **8**, 4200–4213 (2006).
45. Ramírez, P., Mafe, S., Alcaraz, A. & Cervera, J. Modeling of pH-switchable ion transport and selectivity in nanopore membranes with fixed charges. *J. Phys. Chem. B* **107**, 13178–13187 (2003).
46. Adamson, A. W. *A Textbook of Physical Chemistry* 2nd edn (Academic Press, 1979).
47. Wu, D. et al. Computational exploration of Zr-carboxylate based metal–organic framework as a membrane material for CO_2 capture. *J. Mater. Chem. A* **2**, 1657–1661 (2014).
48. Mayo, S. L., Olafson, B. D. & Goddard, W. A. DREIDING: a generic force field for molecular simulations. *J. Phys. Chem.* **94**, 8897–8909 (1990).
49. Rappé, A. K., Casewit, C. J., Colwell, K., Goddard, W. A. III & Skiff, W. M. Uff, a full periodic table force field for molecular mechanics and molecular dynamics simulations. *J. Am. Chem. Soc.* **114**, 10024–10035 (1992).
50. Li, P., Roberts, B. P., Chakravorty, D. K. & Merz, K. M. Jr Rational design of particle mesh Ewald compatible Lennard-Jones parameters for +2 metal cations in explicit solvent. *J. Chem. Theory Comput.* **9**, 2733–2748 (2013).
51. Li, P., Song, L. F. & Merz, K. M. Jr Systematic parameterization of monovalent ions employing the nonbonded model. *J. Chem. Theory Comput.* **11**, 1645–1657 (2015).
52. Fiorin, G., Klein, M. L. & Hénin, J. Using collective variables to drive molecular dynamics simulations. *Mol. Phys.* **111**, 3345–3362 (2013).

Acknowledgements

This project is supported by the Australian Research Council (grant nos. DP180100298, DE170100006, DP170102964 and DP180102890). J.L. thanks the Chinese Scholarship Council for a PhD scholarship. J.Z.L. thanks the start-up fund from The University of Melbourne. G.J. thanks the National Natural Science Foundation of China (grant no. 21905215) for support. B.D.F.'s work is supported by the Center for Materials for Water and Energy Systems (M-WET), an Energy Frontier Research Center funded by the US Department of Energy, Office of Science, Office of Basic Energy Sciences under Award No. DE-SC0019272. We acknowledge assistance from B.Qian and X.Chen in the experiments and use of the facilities and assistance from Y.Chen and X.Fang in the Monash Center for Electron Microscopy. We also acknowledge the assistance of resources and services from the National Computational Infrastructure, which is

supported by the Australian Government. We acknowledge the assistance of P. Cook in editing the manuscript.

Author contributions

H.Z. conceived the project concept. H.Z. and H.W. designed the detailed project scope. H.Z. and J.L. designed the experiments. J.L. and H.Z. performed the sample preparation. J.L. conducted sample measurements and characterizations. G.J. conducted the MD simulations under the guidance of J.Z.L. J.H., X.L., X.H. and Y.H. helped conduct the SEM, PXRD and Zeta potential measurements. C.D.E. carried out the XPS analysis. C.S. and Q.L. did the DFT calculations. J.L. and H.Z. analysed the data and wrote the paper. B.D.F., A.J.H., A.W.T., M.R.H., X.Z., L.J. and H.W. discussed the results and commented on the manuscript. H.Z., J.L., G.J., J.Z.L. and H.W. revised the manuscript. H.Z. and H.W. supervised the work.

Competing interests

H.Z., H.W., X.L., J.L., B.D.F. and A.J.H. are inventors on an international patent application related to this work filed by Monash University (application no. PCT/AU2018/051341). All other authors have no competing interests.

Additional information

Supplementary information is available for this paper at https://doi.org/10.1038/s41563-020-0634-7.

Correspondence and requests for materials should be addressed to H.Z., G.J. or H.W.

Reprints and permissions information is available at www.nature.com/reprints.